CHEMISTRY OF MATERIALS

Article

pubs.acs.org/cm

In Operando Probing of Sodium-Incorporation in NASICON Nanomaterial: Asymmetric Reaction and Electrochemical Phase Diagram

Guobin Zhang,[†,§] Tengfei Xiong,[†,§] Mengyu Yan,[*,†,‡] Yanan Xu,[†] Wenhao Ren,[†] Xu Xu,[†] Qiulong Wei,[†] and Liqiang Mai[*,†,∥]

[†]State Key Laboratory of Advanced Technology for Materials Synthesis and Processing, International School of Materials Science and Engineering, Wuhan University of Technology, Wuhan 430070, P. R. China

[‡]Materials Science and Engineering Department, University of Washington, Seattle, Washington 98195-2120, United States

[∥]Department of Chemistry, University of California, Berkeley, California 94720, United States

Supporting Information

ABSTRACT: NASICON-type materials are one of the most promising cathodes for sodium-ion batteries (SIBs) due to their stable structure and the three-dimensional framework for the migration of Na^+. During the usage of SIBs, they should hold the ability to endure sudden changes in temperature and current density, which have a profound impact on battery life. However, little research focused on the reaction mechanism under the above situations. Here, the phase transformation processes of NASICON-type material, $Na_3V_2(PO_4)_3$, are investigated by applying high-resolution in situ X-ray diffraction and Raman coupled with electrochemical tests under different temperatures (273 and 293 K) and scan rates (0.5, 2, and 5 mV s^{-1}). The results demonstrate that the phase evolution process is one-phase solid solution during the desodiation process rather than the traditionally two-phase reaction at a high scan rate or low temperature. An electrochemical phase diagram is also drawn based on thein situ results, which can be used to explain the asymmetric result. This work can help with understanding the phase evolution process of NASICON-type cathodes, as well as guiding the application of SIBs in various working conditions.

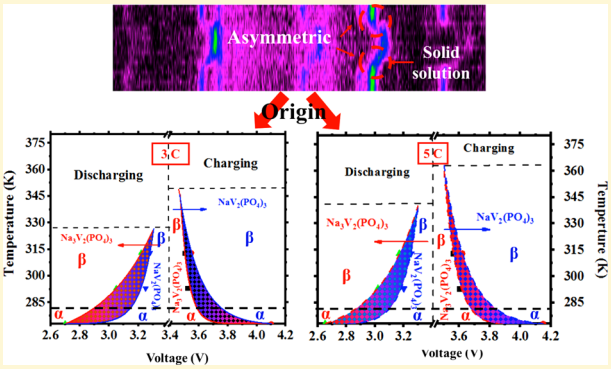

1. INTRODUCTION

Due to abundant resources, low cost,and competitive energy densities, sodium-ion batteries (SIBs) have attracted much attention in sustainable development as well as large-scale applications to realize the utilization of reducing the peaks and filling the valleys in the power grid.[1,2] Fast Na^+ superionic conductor (NASICON)-related compounds, as one of the typical sodium cathode materials, are of great interest due to their three-dimensional sodium transfer pathway.[3,4] These NASICON-type materials were first studied as the solid electrolyte by a few researchers such as Goodenough, Hong, and Delmas.[5−7] Then, they were reinvestigated for their stable structure and sodium deinsertion.[8]

The NASICON-type materials are typically constructed by the isolated octahedral and tetrahedral units, which often lead to the low intrinsic electronic conductivity.[9,10] Maya et al. overcame this drawback by using optimizing strategies such as nanosizing and carbon coating.[11,12] There is also some literature reporting the electrochemical reaction mechanism of NASICON-type materials at relatively low current densities. Lim et al. used ex situ X-ray diffraction (XRD) to investigate the reaction mechanism at 0.2 C and found the two-phase reaction mechanism, which was further proved by Jian et al. with the employment of in situ XRD at 0.1 C.[13,14] However, the utilization of NASICON-type materials is faced with various operating environments, including different charge/discharge rates and temperatures, which have not been fully studied. More importantly, the reaction mechanisms of NASICON-type materials and the corresponding dynamic behavior at different rates, which is hidden in the electrochemical process, have not ever been explored at different reaction temperatures.

Here, $Na_3V_2(PO_4)_3$ is selected to systematically study the reaction mechanism of NASICON-type materials under different reaction conditions (scan rates of 0.5, 2, and 5 mV s^{-1}, temperatures of 273 and 293 K) by applying in situ XRD, Raman, and electrochemical tests. The phase evolution process turns out to be an asymmetric transformation process, where a one-phase solid solution reaction occurs during the anodic process and a two-phase evolution is observed during the cathodic period. The electrochemical phase diagram is drawn

Received: March 8, 2017
Revised: September 13, 2017
Published: September 13, 2017

DOI: 10.1021/acs.chemmater.7b00957
Chem. Mater. 2017, 29, 8057−8064

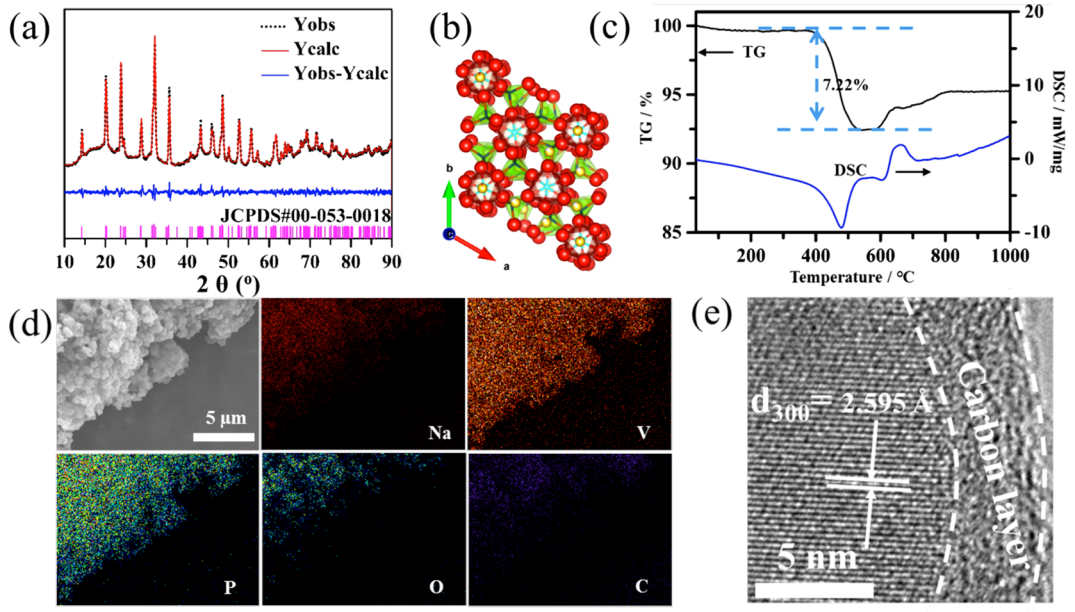

Figure 1. Characterizations of the as-synthesized material. (a) XRD pattern and Rietveld refinement of $Na_3V_2(PO_4)_3$/C. (b) Crystal structure of hexagonal $Na_3V_2(PO_4)_3$ along the *c* axis (yellow: Na; cyan: V; dark blue: P; red: O). (c) TG-DSC curve of $Na_3V_2(PO_4)_3$/C at room temperature to 1000 °C. (d) Elemental mapping images of the $Na_3V_2(PO_4)_3$/C particles and (e) HRTEM image.

based on the operando results (3 C and 5 C at 273, 293, and 313 K, where 1 C refers to 117 mA g^{-1} for $Na_3V_2(PO_4)_3$). With the help of the electrochemical phase diagram, it is possible to understand the phase evolution process of NASICON-type material to promote the development of SIBs. This work can help the understanding of the functioning of this polyanionic electrode material in real operating conditions.

2. EXPERIMENTAL SECTION

2.1. Materials Synthesis. The $Na_3V_2(PO_4)_3$/C particles were synthesized according to the literature.[15] The main reagents NaH_2PO_4, $H_2C_2O_4{\cdot}2H_2O$, and V_2O_5 were analytical grade, purchased from Sinopharm Chemical Reagent Co., Ltd. (Shanghai, China). First, V_2O_5 (1 mmol) and $H_2C_2O_4{\cdot}2H_2O$ (3 mmol) were dissolved in H_2O (15 mL), and the system was stirred for 30 min at 70 °C. Then, NaH_2PO_4 (3 mmol) and glucose (1 mmol) were added to the above solution with vigorous stirring for 10 min. Afterward, dimethylformamide (50 mL) was added drop by drop, followed by stirring for 10 min. Next, the solution was dried at 70 °C for 24 h to obtain the precursor. Finally, the $Na_3V_2(PO_4)_3$/C particles were obtained after the preheating process at 400 °C for 4 h and the annealing process at 750 °C for 8 h in Ar, with a heating rate of 5 °C min^{-1}.

2.2. Materials Characterization. The images of morphology and microstructure were collected by a JEOL-7100F microscope and a JSM-2010 microscope, respectively. Element mapping was obtained via an EDX-GENESIS 60S spectrometer. XRD characterization of the powder sample and in situ XRD tests of the cathode sheet were carried out with a Bruker D8 Discover X-ray diffractometer, using Cu Kα radiation (λ = 1.5418 Å). XRD refinement was conducted with the software TOPAS. Figure S1 (Supporting Information)[16] shows the schematic of the in situ cell. TG-DSC curves were obtained using a Netzsch STA 449C thermal analyzer with a heating rate of 10 K min^{-1} in air. BET (Brunauer–Emmet–Teller) surface area was calculated from nitrogen adsorption isotherms at 77 K by using a Tristar II 3020 instrument. Raman spectra were obtained via a Renishaw INVIA micro-Raman spectroscopy system.

2.3. Electrochemical Measurements. The 2016 coin cells were assembled in a glovebox filled with pure argon. When sodium foil was used as the anode, the electrolyte was composed of 1 M $NaClO_4$ in ethylene carbonate/dimethyl carbonate (1:1 w/w) with 5 wt % fluoroethylene carbonate (FEC) additive. The glass fiber was used as the separator. The cathode was obtained with 70% active material, 20% acetylene black, and 10% poly(tetrafluoroethylene) (PTFE) binder. The assembly of in situ cells was similar, except that the Be window was used. Galvanostatic charge/discharge cycling was studied from 2.3 to 4.2 V vs Na^+/Na using a multichannel battery testing system (LAND CT2001A). The in situ XRD signals were collected using the VANTEC-500 detector in a still mode during the discharge–charge process, and each pattern took 30 s to acquire. CV (cyclic voltammetry) and EIS (electrochemical impedance spectroscopy) were obtained with an electrochemical workstation (Autolab PGSTAT302N).

3. RESULTS AND DISCUSSION

The powder XRD and further Rietveld refinement implemented by TOPAS 4.2 (a relatively low Rwp value of 3.11% is achieved) are employed to investigate the crystal structure of $Na_3V_2(PO_4)_3$ (Figure 1a). The Rietveld result shows that the as-synthesized material is hexagonal with a space group of $R\bar{3}c$ (lattice parameter of $a = b = 8.748$ Å, $c = 21.852$ Å, $\alpha = \beta = 90°$, $\gamma = 120°$) and a crystal size of 80.3 nm. The P–O tetrahedral and the V–O octahedral form the structure shown in Figure 1b. Thermogravimetry analysis (TGA) is applied, and the TG curve (Figure 1c) proves that the content of carbon is ~7.22%. The scanning electron microscopy (SEM) (Figure 1d) shows the as-synthesized material consists of small nanosized particles. These elements are evenly distributed as shown in the energy dispersive X-ray spectroscopic (EDS) (Figure 1d) mapping of the material. To further investigate the carbon-coating of the as-synthesized material, high resolution transmission electron microscopy (HRTEM) is employed (Figure 1e), and the HRTEM image clearly shows that the thickness of the carbon shell is ~5 nm. The HRTEM image and the XRD fitting result prove that the preferred orientation of $Na_3V_2(PO_4)_3$ nanomaterial is a (300) lattice plane with a space distance of 2.59 Å. The BET (Brunauer–Emmet–Teller) result (Figure S2, Supporting Information) shows that the specific surface area of the powder is 76.9 m^2 g^{-1}. The as-synthesized material

DOI: 10.1021/acs.chemmater.7b00957
Chem. Mater. 2017, 29, 8057–8064

delivers a capacity of 80 mA h g^{-1} after 1000 cycles at 5 C (Figure S3, Supporting Information).

To study the phase transition mechanism at different temperatures, DSC measurement was done for $Na_3V_2(PO_4)_3$ and $NaV_2(PO_4)_3$ in the temperature range of 213−373 K at the heating rate of 10 K min^{-1} as shown in Figure 2.[17]

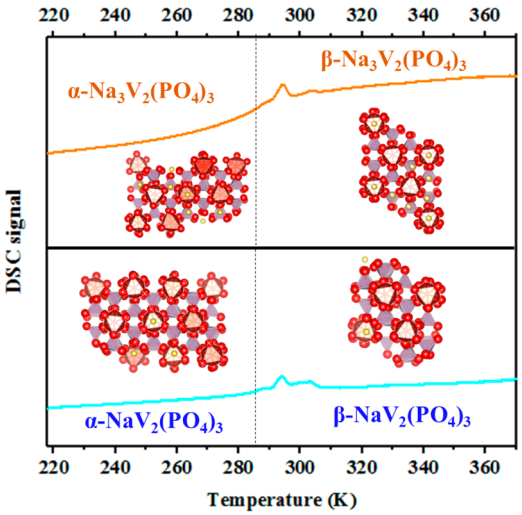

Figure 2. DSC measurement of $Na_3V_2(PO_4)_3$ and $NaV_2(PO_4)_3$ (four different crystal structures) from 213 to 373 K (10 K min^{-1}).

$Na_3V_2(PO_4)_3$ undergoes a distinct phase transition from α-$Na_3V_2(PO_4)_3$ to β-$Na_3V_2(PO_4)_3$, and $NaV_2(PO_4)_3$ undergoes a distinct phase transition from α-$NaV_2(PO_4)_3$ to β-$NaV_2(PO_4)_3$. As reported, the phase transition from α-$Na_3V_2(PO_4)_3$ to β-$Na_3V_2(PO_4)_3$ happens at around 283 K; thus, in situ XRD of $Na_3V_2(PO_4)_3$ and $NaV_2(PO_4)_3$ at temperatures of 273, 283, and 293 K in the in situ cell was collected for 5 min per pattern (Figure S4, Supporting Information). The results show that the phase transitions of $Na_3V_2(PO_4)_3$ and $NaV_2(PO_4)_3$ happen at around 283 K. To further determine the crystal structure of these four phases, XRD patterns of the two phases at 273 and 293 K were done for 6 h per pattern (Figure S5, Supporting Information). With declining the temperature, the peak at ∼32° shifts to the higher diffraction angle, which indicates the shrinkage of the crystal. From the selected range of the XRD patterns in Figure S5, the peak splitting phenomenon is apparent at 273 K for both $Na_3V_2(PO_4)_3$ and $NaV_2(PO_4)_3$, which shows the same character as that in the literature.[17] Further XRD refinement is done to get the crystal information (Figure S6, Supporting Information). The refinement results show that the high-site symmetry phase with space group of *R*/3*c* turns to a low-site symmetry phase of *C*2/*c* at ∼283 K for $Na_3V_2(PO_4)_3$ and $NaV_2(PO_4)_3$.

In situ XRD was performed at different scan rates of 0.5, 2, and 5 mV s^{-1} (Figure 3a−c) under an ambient condition (293 K) to investigate the phase transformation process. At a low

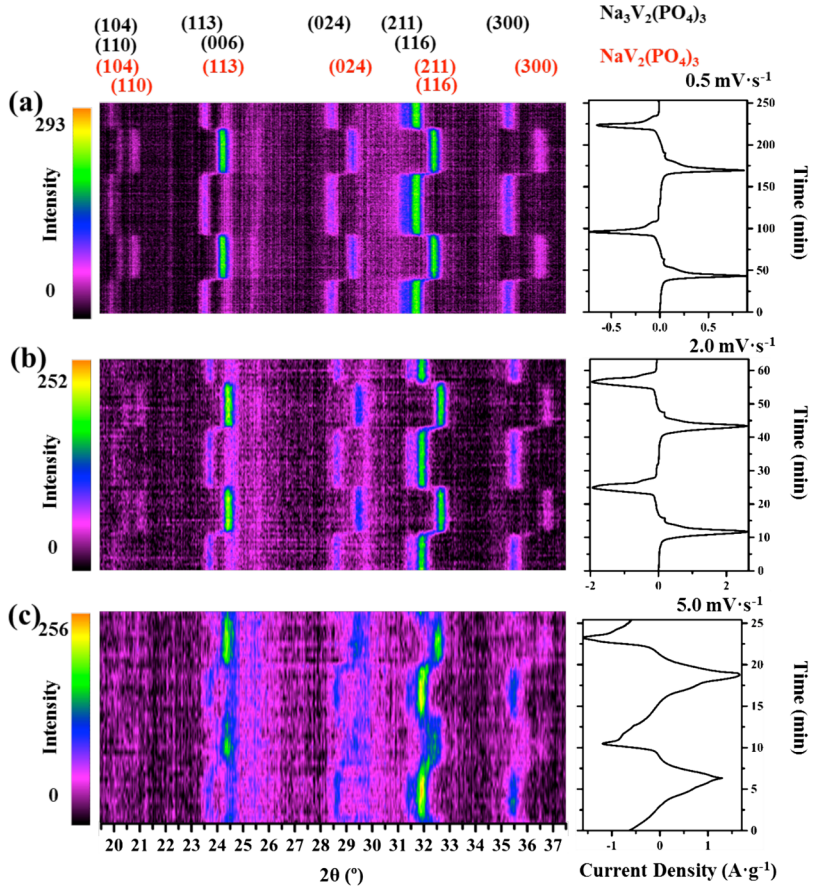

Figure 3. Two-dimensional in situ XRD patterns of β-$Na_3V_2(PO_4)_3$/C during the CV processes in the voltage range of 2.3−4.2 V at 293 K. Four peak regions (with lattice planes marked above the patterns) can be observed with the two theta range of 19.5−37.5°. The diffraction intensity is coded with different colors shown in the scale bar on the left. Time−current density plots are shown on the right. Corresponding scan rates are (a) 0.5, (b) 2.0, and (c) 5.0 mV s^{-1}, respectively.

DOI: 10.1021/acs.chemmater.7b00957
Chem. Mater. 2017, 29, 8057−8064

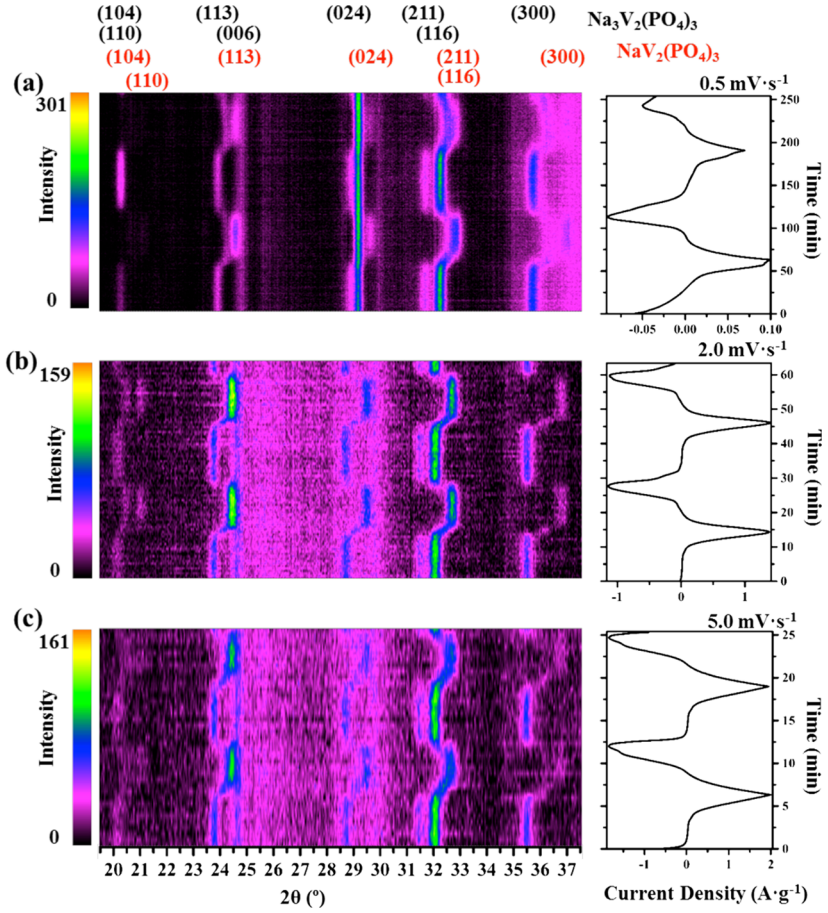

Figure 4. Two-dimensional in situ XRD patterns of α-$Na_3V_2(PO_4)_3$ during the CV processes with the voltage range of 2.3−4.2 V at 273 K. Four peak regions (with lattice planes marked above the patterns) can be observed with the two theta range of 19.5−37.5°. The diffraction intensity is coded with different colors shown in the scale bar on the left. Corresponding scan rates are (a) 0.5, (b) 2.0, and (c) 5.0 mV s^{-1}, respectively. The neglected peaks between the two stable phases become more distinct at 273 K.

scan rate of 0.5 mV s^{-1} (Figure 3a), all diffraction peaks can be indexed to $Na_3V_2(PO_4)_3$ and $NaV_2(PO_4)_3$ with two theta angle ranging from 19.5° to 37.5°. These experiment results are consistent with former work and traditional understanding: the diffraction peaks of $Na_3V_2(PO_4)_3$ disappear while the peaks of $NaV_2(PO_4)_3$ appear suddenly.[14] As the scan rate increases to 2 mV s^{-1} (Figure 3b), continuous positive intensities appear in the selected angle ranges, suggesting that observable phases appear during the anodic period and negligibly during the cathodic process. When the scan rate increases to 5 mV s^{-1} (Figure 3c), continuous strong positive intensities move to the peaks indexed to $NaV_2(PO_4)_3$ during the anodic period. And during the cathodic process, the strong positive intensities move to the diffraction peaks of $Na_3V_2(PO_4)_3$ with negligible breaks. This asymmetric result indicates that the phase evolution process becomes different compared with the result at 0.5 mV s^{-1}, where the phase transformation in the anodic progress turns out to be a solid solution reaction with the increscent scan rate. This result indicates the transformation mechanism changes from the traditional two-phase transformation to a one-phase solid solution reaction.

There is little research studying the mechanism of α-$Na_3V_2(PO_4)_3$ at low temperature. To study the low temperature reaction mechanism, in situ XRD measurements with the CV scan rates of 0.5, 2.0, and 5.0 mV s^{-1} (Figure 4a−c, respectively) are performed at 273 K. It is found that the asymmetric reaction becomes more obvious. Positive intensities of the diffraction peaks of α-$Na_3V_2(PO_4)_3$ gradually move to the peaks of α-$NaV_2(PO_4)_3$ during the anodic reaction and jump with negligible intensities to $Na_3V_2(PO_4)_3$ during the cathodic process at the scan rates of 0.5 and 2 mV s^{-1}. At a high scan rate of 5.0 mV s^{-1}, the process from α-$NaV_2(PO_4)_3$ to α-$Na_3V_2(PO_4)_3$ becomes different.

Pawley XRD refinement solution was employed to explore the lattice parameter changes (Figure 5a−h) resulting from different temperatures (273 and 293 K) and different scan rates (0.5 and 5 mV s^{-1}).[18,19] At the scan rate of 0.5 mV s^{-1} (Figure 4a−d), β-$Na_3V_2(PO_4)_3$ with lattice parameters of about $a = b =$ 8.748 Å and $c =$ 21.852 Å abruptly transforms to a sodium-deficient phase with lattice parameters of about $a = b =$ 8.507 Å and $c =$ 21.713 Å, which indicates the two-phase transition mechanism. Then the sodium-deficient phase changes back to the original one with the instantaneous increase of lattice parameters during the discharge process (Figure 5a,c). However, at 5 mV s^{-1}, lattice parameters of the pristine gradually shift with a gentle slope to the sodium-deficient phase during both the anodic and the cathodic electrochemical processes at 293 K (Figure 5e,g). This result indicates the transformation mechanism changes from the traditional two-phase transformation to one-phase solid solution reaction. At 273 K and 0.5 mV s^{-1}, α-$Na_3V_2(PO_4)_3$ with lattice parameters of about $a =$ 15.037, $b =$ 8.662 Å, $c =$ 21.660 Å, and $\beta =$ 90.169°

DOI: 10.1021/acs.chemmater.7b00957
Chem. Mater. 2017, 29, 8057−8064

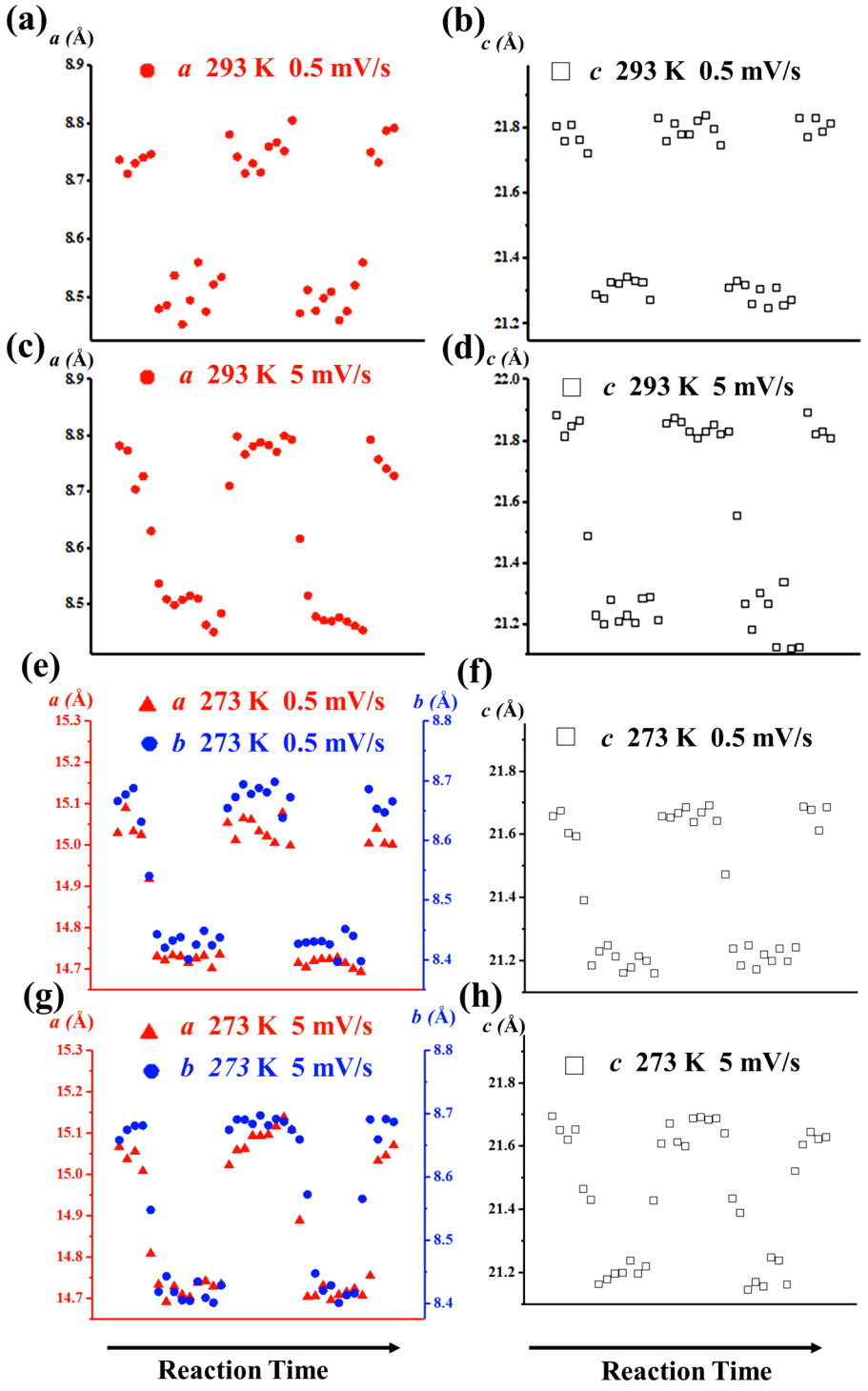

Figure 5. Average lattice parameter changes of *a*, *b*, and *c* (a, b, e, and f at 293 K and c, d, g, and h at 273 K) during the CV processes calculated from in situ XRD patterns in Figures 3 and 4. As the temperature decreases to 273 K (Figure 4f,h), the lattice parameter changes as well as the asymmetric phenomenon.

abruptly transforms to sodium-deficient phase with lattice parameters of about a = 14.757, b = 8.472 Å, c = 21.212 Å, and β = 90.248°. As the temperature declines to 273 K (Figure 5f,h), lattice parameter changes as well as the asymmetric phenomenon, which are pointed out in the dotted rectangle, become more obvious. The assumption is that the asymmetric reaction may have the different sodium-ion diffusion coefficients. The superstructure of α-$Na_3V_2(PO_4)_3$ may accelerate the sodium transportation in the superlattice structure due to the stability of the structure.

To further understand the phenomenon above, sodium ion diffusion coefficients in the electrochemical processes at different temperatures (253, 273, 293, 313, and 333 K) are deduced through CV curves at different scan rates (1, 2, 5, and 10 mV s^{-1}), which might be helpful to understand the mechanism quantitatively (Figure 6a–e). The voltage difference between the oxidation peak and reduction peak increases

DOI: 10.1021/acs.chemmater.7b00957
Chem. Mater. 2017, 29, 8057–8064

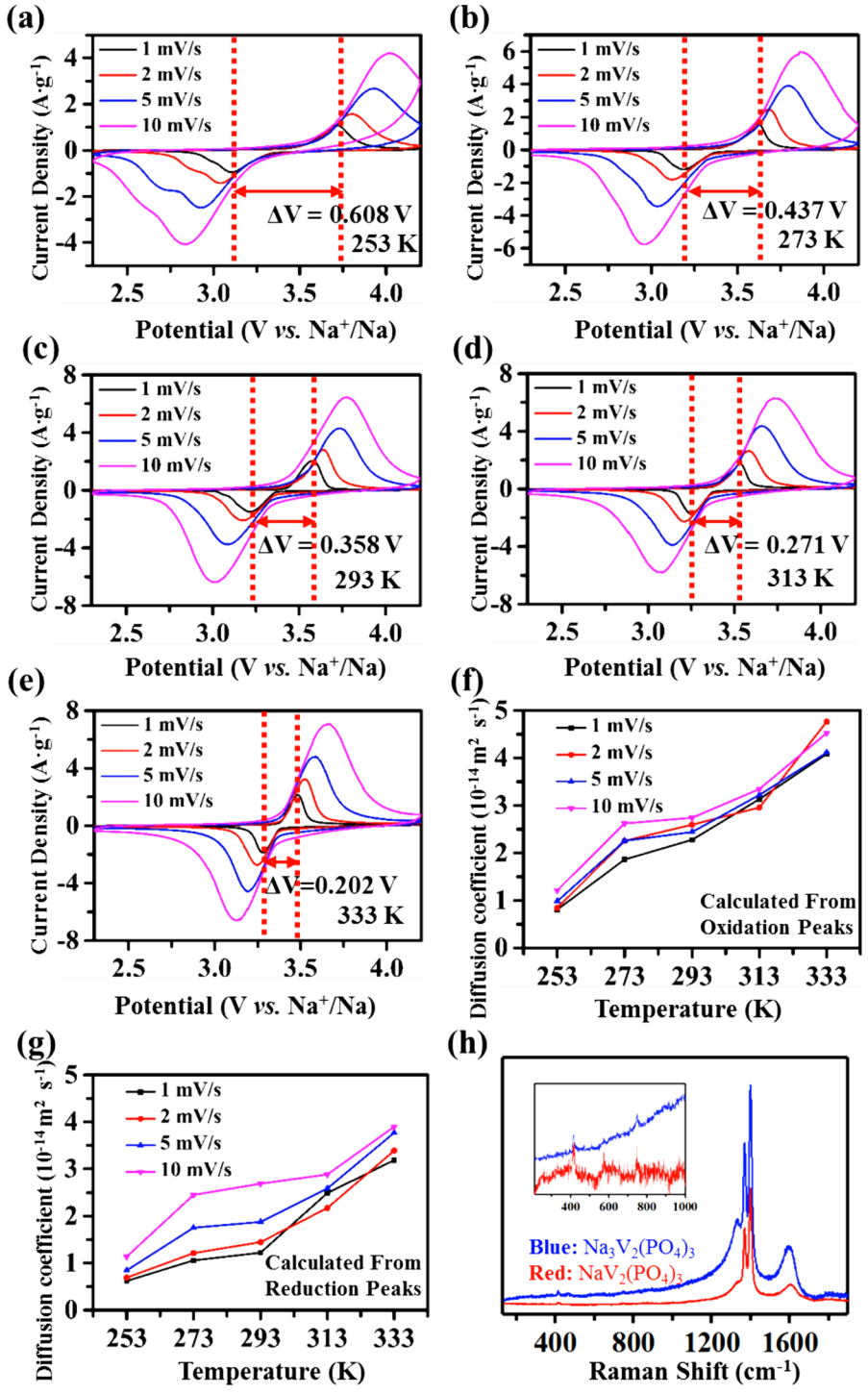

Figure 6. CV curves of $Na_3V_2(PO_4)_3$ at temperatures (a)253 K, (b) 273 K, (c) 293 K, (d) 313 K, and (e) 333 K and scan rates 1, 2, 5, and 10 mV s^{-1}, respectively. The diffusion coefficient calculated from (f) oxidation peaks and (g) reduction peaks of $Na_3V_2(PO_4)_3$ at different scan rates and different temperatures; (h) the Raman shifts of $Na_3V_2(PO_4)_3$ and $NaV_2(PO_4)_3$. (The inset plot is the selected region of 100−1000 cm^{-1}.)

from 0.202 to 0.608 V with the decrease of the temperature from 333 to 253 K at 1 mV s^{-1}. The sodium ion diffusion coefficients are determined according to the Randles−Sevchik equation for the semi-infinite diffusion of Na^+ into or out of the chemical host.[20,21] The calculated diffusion coefficients from oxidation and reduction peaks decrease by reducing the temperature (Figure 6f,g). But the decreasing trend of the diffusion coefficient has a gentle dip at 293 K, which indicates that there may exist different reaction mechanisms or different reaction pathways during the electrochemical process around 293 K. Raman shifts of the charged as well as the discharged state of $Na_3V_2(PO_4)_3$ are presented in Figure 6h to study the chemical bond variation within a Raman shift range of 200−3000 cm^{-1}. A detailed image with a range of 200−1000 cm^{-1} in the inset plot of Figure 6h indicates that there is no peak shift. Two intense bands at ∼750 and 550 cm^{-1} and one strong band at ∼420 cm^{-1} can be indexed to the vibrations and bending modes of $[VO_6]$ octahedron and $[PO_4]$ tetrahedral.[22]

DOI: 10.1021/acs.chemmater.7b00957
Chem. Mater. 2017, 29, 8057−8064

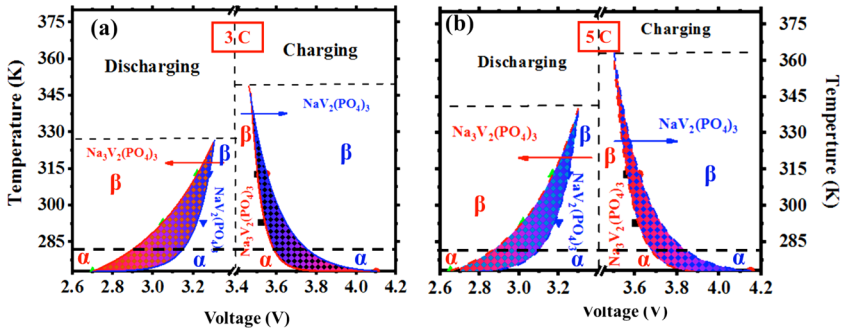

Figure 7. Phase diagrams of $Na_3V_2(PO_4)_3$ during galvanostatic charge and discharge at different current rates of (a) 3 C and (b) 5 C. In each phase diagram, the horizontal axis represents the voltage range, and temperature is on the vertical axis.

Furthermore, carbon materials can be obviously observed by two characteristic bands: D-band around 1360 cm^{-1} and G-band around 1600 cm^{-1}, which is mixed with the band of corundum around 1367 and 1399 cm^{-1}. In situ Raman measurement is employed to characterize the reaction pathway within the Raman shift range from 200 to 1000 cm^{-1} at a current density of 1 C (Figure S7, Supporting Information). The asymmetric reaction pathway still exists in the in situ Raman results. From the one-dimensional image (Figure S7a), the band around 420 cm^{-1} presents no changes, while the bands around 750 and 550 cm^{-1} become weaker and weaker. All the peaks can recover to its original state as the material returns to its discharged state. The wo dimensional image of the in situ Raman spectrum (Figure S7b) shows that the intensity changes little during the charge process but changes greatly during the discharge process within the band range from 550 to 750 cm^{-1}. Meanwhile, strong positive intensities appear within the same range during the discharge process highlighted by the dashed line. In conclusion, the cathodic process can be transformed more quickly compared with the anodic process due to the solid state reaction, which is captured in the in situ XRD and in situ Raman results. The asymmetric reaction pathway observed in our work can accelerate the sodium ion diffusion and thus mitigate the decrement of the sodium ion diffusion coefficient with the decline of temperature.

In situ XRD of $Na_3V_2(PO_4)_3$ at the rates 3 and 5 C and the temperatures 273, 293, and 313 K was performed (Figure S8, Supporting Information) to further investigate the electrochemical reaction mechanism. The result also shows the existence of the asymmetric reaction pathway, which highly consists with the in situ XRD results at different scan rates. To further study the existent condition of the solid solution reaction in such a polyanion-type system, the electrochemical phase diagram of charging and discharging processes is drawn (Figure 7a,b) based on the acquired date from Figure S8. The occurrence of the solid solution and the formation of the stable charged or discharged phase is regarded as the starting and the ending point. In the in situ date, the slight peak shift point from the pristine or sodium poor phase is selected, from where the voltage and the temperature parameters can be acquired. The formation and development of the solid solution reaction can be deduced from the acquired data, which follows the trend of exponent decay or growth during the charging or discharging process. It can be observed from the deduced electrochemical phase diagram that the reaction is asymmetric and there exists different reaction pathways. With the help of the fitted electrochemical phase diagram, the electrochemical property of this solid solution and the asymmetric reaction can be easily traced. To study the character of the solid solution process, the charge-relax experiment was employed at 273 and 293 K where a current equivalent to 10 C is applied for 90 s followed by an open-circuit relaxation of 10 min (Figure S9, Supporting Information). The electrochemical process presents the solid solution reaction at an elevated current density, which is induced by the overpotential. At low temperature, the occurrence of the asymmetric reaction becomes more obvious, where temperature is the dominant factor rather than current density. This material system shows the similarity with the $LiFePO_4/FePO_4$ system. Compared with our previous work, this material system is more complicated and interesting.[23] The $LiFePO_4/FePO_4$ system shows no phase transition induced by temperature during 273−293 K. This is due to the not fully occupied site position of the sodium in the $Na_3V_2(PO_4)_3$ structure.

4. CONCLUSIONS

The phase transition processes of sodium ion cathode material, $Na_3V_2(PO_4)_3$, are investigated at different CV scan rates (0.5, 2, and 5 mV s^{-1}) and temperatures (273 and 293 K) under operando conditions, where the asymmetric reaction routes are observed. The nonlinear decline trend of the calculated sodium ion diffusion coefficients confirms the existence of the asymmetric reaction. The in situ XRD result at different current densities of 3 and 5 C and temperatures 273, 293, and 333 K and further in situ Raman result are consistent with the assumption. The experiment result shows that the solid solution reaction can accelerate the phase transformation process. The electrochemical phase diagram of $Na_3V_2(PO_4)_3$ is drawn to understand the property of the asymmetric reaction in NASICON-type material at different temperatures. These observations and analyses can help in the understanding and development of the next generation SIBs with enhanced rate capability and better temperature adaptability.

■ ASSOCIATED CONTENT

Supporting Information

The Supporting Information is available free of charge on the ACS Publications website at DOI: 10.1021/acs.chemmater.7b00957.

Experiment device, procedures, cycle performances, powder patterns, and Raman spectrum (PDF)

■ AUTHOR INFORMATION

Corresponding Authors

*(M.Y.) E-mail: ymymiles@whut.edu.cn.

DOI: 10.1021/acs.chemmater.7b00957
Chem. Mater. 2017, 29, 8057−8064

*(L.M.) E-mail: mlq518@whut.edu.cn.

ORCID

Qiulong Wei: 0000-0002-9551-8309

Liqiang Mai: 0000-0003-4259-7725

Author Contributions

§G. Zhang and T. Xiong contributed equally to this work.

Notes

The authors declare no competing financial interest.

■ ACKNOWLEDGMENTS

This work was supported by the National Key Research and Development Program of China (2016YFA0202603), the National Basic Research Program of China (2013CB934103), the Program of Introducing Talents of Discipline to Universities (B17034), the National Natural Science Foundation of China (51521001, 51602239), the National Natural Science Fund for Distinguished Young Scholars (51425204), the Fundamental Research Funds for the Central Universities (WUT 2017-YB-005), and the Fundamental Research Funds for the Central Universities (WUT: 2016III001, 2016III003, 2016IVA090). L.Q.M. gratefully acknowledges financial support from the China Scholarship Council (No.201606955096). M.Y. Yan would like to acknowlege the support from the State of Washington through the Universtity of Washington Clean Energy Institute. The authors thank Prof. Massimo Nespolo of Université de Lorraine for strong support and stimulating discussion.

■ REFERENCES

(1) Fang, C.; Huang, Y. H.; Zhang, W. X.; Han, J. T.; Deng, Z.; Cao, Y. L.; Yang, H. X. Routes to High Energy Cathodes of Sodium-Ion Batteries. *Adv. Energy Mater.* **2016**, *6* (5), 1501727.

(2) Palacin, M. R.; de Guibert, A. Why do batteries fail? *Science* **2016**, *351* (6273), 1253292.

(3) Kabbour, H.; Coillot, D.; Colmont, M.; Masquelier, C.; Mentre, O. alpha-$Na_3M_2(PO_4)_3$ (M = Ti, Fe): absolute cationic ordering in NASICON-type phases. *J. Am. Chem. Soc.* **2011**, *133* (31), 11900−11903.

(4) Kang, J.; Baek, S.; Mathew, V.; Gim, J.; Song, J.; Park, H.; Chae, E.; Rai, A. K.; Kim, J. High rate performance of a $Na_3V_2(PO_4)_3$/C cathode prepared by pyro-synthesis for sodium-ion batteries. *J. Mater. Chem.* **2012**, *22* (39), 20857−20860.

(5) Goodenough, J. B.; Hong, H. Y. P.; Kafalas, J. A. Fast Na+-ion transport in skeleton structures. *Mater. Res. Bull.* **1976**, *11* (2), 203−220.

(6) Hong, H. Y. P. Crystal structures and crystal chemistry in the system $Na_{1+x}Zr_2SixP_{3-x}O_{12}$. *Mater. Res. Bull.* **1976**, *11* (2), 173−182.

(7) Delmas, C.; Nadiri, A.; Soubeyroux, J. L. The nasicon-type titanium phosphates $ATi_2(PO_4)_3$ (A= Li, Na) as electrode materials. *Solid State Ionics* **1988**, *28*, 419−423.

(8) Plashnitsa, L. S.; Kobayashi, E.; Noguchi, Y.; Okada, S.; Yamaki, J. Performance of NASICON Symmetric Cell with Ionic Liquid Electrolyte. *J. Electrochem. Soc.* **2010**, *157* (4), A536−A543.

(9) Bianchini, M.; Brisset, N.; Fauth, F.; Weill, F.; Elkaim, E.; Suard, E.; Masquelier, C.; Croguennec, L. $Na_3V_2(PO_4)_2F_3$ Revisited: A High-Resolution Diffraction Study. *Chem. Mater.* **2014**, *26* (14), 4238−4247.

(10) Lu, Y. C.; Ma, C.; Alvarado, J.; Dimov, N.; Meng, Y. S.; Okada, S. Improved electrochemical performance of tin-sulfide anodes for sodium-ion batteries. *J. Mater. Chem. A* **2015**, *3* (33), 16971−16977.

(11) An, Q. Y.; Xiong, F. Y.; Wei, Q. L.; Sheng, J. Z.; He, L.; Ma, D. L.; Yao, Y.; Mai, L. Q. Nanoflake-Assembled Hierarchical $Na_3V_2(PO_4)_3$/C Microflowers: Superior Li Storage Performance and Insertion/Extraction Mechanism. *Adv. Energy Mater.* **2015**, *5* (10), 1401963−1401973.

(12) Chu, Z.; Yue, C. Core−shell structured $Na_3V_2(PO_4)_3$/C nanocrystals embedded in multi-walled carbon nanotubes: A high-performance cathode for sodium-ion batteries. *Solid State Ionics* **2016**, *287*, 36−41.

(13) Lim, S. Y.; Kim, H.; Shakoor, R. A.; Jung, Y.; Choi, J. W. Electrochemical and Thermal Properties of NASICON Structured $Na_3V_2(PO_4)_3$ as a Sodium Rechargeable Battery Cathode: A Combined Experimental and Theoretical Study. *J. Electrochem. Soc.* **2012**, *159* (9), A1393−A1397.

(14) Jian, Z.; Han, W.; Lu, X.; Yang, H.; Hu, Y.-S.; Zhou, J.; Zhou, Z.; Li, J.; Chen, W.; Chen, D.; Chen, L. Superior Electrochemical Performance and Storage Mechanism of $Na_3V_2(PO_4)_3$ Cathode for Room-Temperature Sodium-Ion Batteries. *Adv. Energy Mater.* **2013**, *3* (2), 156−160.

(15) Ren, W.; Yao, X.; Niu, C.; Zheng, Z.; Zhao, K.; An, Q.; Wei, Q.; Yan, M.; Zhang, L.; Mai, L. Cathodic polarization suppressed sodium-ion full cell with a 3.3V high-voltage. *Nano Energy* **2016**, *28*, 216−223.

(16) Zhang, G.; Xiong, T.; He, L.; Yan, M.; Zhao, K.; Xu, X.; Mai, L. Electrochemical *in-situ* X-ray probing in lithium-ion and sodium-ion batteries. *J. Mater. Sci.* **2017**, *52* (7), 3697−3718.

(17) Chotard, J. N.; Rousse, G.; David, R.; Mentré, O.; Courty, M.; Masquelier, C. (2015). Discovery of a sodium-ordered form of $Na_3V_2(PO_4)_3$ below ambient temperature. *Chem. Mater.* **2015**, *27* (17), 5982−5987.

(18) Pawley, G. S. Unit-cell refinement from powder diffraction scans. *J. Appl. Crystallogr.* **1981**, *14* (6), 357−361.

(19) Brünger, A. T. A memory-efficient fast Fourier transformation algorithm for crystallographic refinement on supercomputers. *Acta Crystallogr., Sect. A: Found. Crystallogr.* **1989**, *45* (1), 42−50.

(20) Trasatti, S.; Petrii, O. A. Real surface area measurements in electrochemistry. *J. Electroanal. Chem.* **1992**, *327* (5), 353−376.

(21) Prosini, P. P.; Lisi, M.; Zane, D.; Pasquali, M. Determination of the chemical diffusion coefficient of lithium in LiFePO4. *Solid State Ionics* **2002**, *148* (1−2), 45−51.

(22) Jian, Z. L.; Zhao, L.; Pan, H. L.; Hu, Y. S.; Li, H.; Chen, W.; Chen, L. Q. Carbon coated $Na_3V_2(PO_4)_3$ as novel electrode material for sodium ion batteries. *Electrochem. Commun.* **2012**, *14* (1), 86−89.

(23) Yan, M. Y.; Zhang, G. B.; Wei, Q. L.; Tian, X. C.; Zhao, K. N.; An, Q. Y.; Zhou, L.; Zhao, Y. L.; Niu, C. J.; Ren, W. H.; He, L.; Mai, L. Q. In operando observation of temperature-dependent phase evolution in lithium-incorporation olivine cathode. *Nano Energy* **2016**, *22*, 406−413.

DOI: 10.1021/acs.chemmater.7b00957
Chem. Mater. 2017, 29, 8057−8064